Synchronized Wireless Measurement of High-Voltage Power System Frequency Using Mobile Embedded Systems

Wenxuan Yao, *Student Member, IEEE*, Haoyang Lu, *Student Member, IEEE*, Micah J. Till, *Student Member, IEEE*, Wei Gao, *Member, IEEE*, and Yilu Liu, *Fellow, IEEE*

***Abstract*—This paper focuses on synchronized wireless measurement of high-voltage (HV) power system frequency using mobile embedded systems (MESs) integrated with a wireless electric field sensor (WEFS). Unlike traditional synchronized frequency measurement devices, which rely on potential transformers and current transformers physically connected to system elements, a WEFS is used to realize wireless signal acquisition in the vicinity of any HV apparatus. The MES performs real-time frequency estimation using a recursive discrete Fourier transform based algorithm. Network time protocol (NTP) is used for time synchronization, increasing the system flexibility by eliminating global positioning system reliance. An NTP-based synchronized sampling control method is proposed and implemented in MES to compensate the sampling time error caused by local time drift and division residue. The proposed system has the advantages of portability and lower cost, making it highly accessible and useful for a wide array of synchronized frequency measurement applications. Experiment results verify the accuracy and effectiveness of the proposed system.**

***Index Terms*—Electric field, high voltage (HV), mobile embedded systems (MESs), network time protocol (NTP), wireless frequency measurement.**

I. Introduction

FREQUENCY, which actually deviates from its nominal value due to imbalances between load and generation, is one of the most critical parameters for monitoring, control, and protection of power systems [1]–[4]. Therefore, accurate frequency measurement plays a significant role in various power system applications such as power quality disturbance detection, power system stabilization, and protection against loss of synchronism [5]–[8].

Due to the extreme vastness and complexity of the power system, it is difficult to be fully monitored via a single measurement device [9]. With the aid of the global positioning system (GPS) for time synchronization, a wide area monitoring system measures the electrical waveforms at multiple power grid nodes using synchronized frequency measurement devices (SFMDs), e.g., phasor measurement units (PMUs), providing the grid operators unprecedented system monitoring and control opportunities [10]. In the past twenty years, SFMDs are increasingly deployed across power systems recording accurate frequency measurements along with unified time stamps [11], [12]. For example, as a pioneer of a synchronized frequency measurement system, a worldwide frequency monitoring network (FNET/Grideye) has been running since 2003 using frequency disturbance recorders (FDRs), members of SFMD family [13]. Applications of synchronized frequency measurement include large area visualization, disturbance detection and location, interarea oscillation mode identification, and postdisturbance scenario reconstruction [14], [15].

A variety of commercial SFMDs, essential elements of wide area frequency measurement systems, are available that assert compliance with industry standards, e.g., IEEE C37.118.1 [16] and IEC 61000-4-30 [17]. However, current SFMDs have several limitations including signal acquisition requirements, GPS reliance, and high costs.

First, to acquire input signal for frequency estimation, SFMDs require direct contact to buses of measurement points through potential transformers (PTs) and current transformers (CTs), which complicates installation and maintenance process and endangers the safety of the personnel, especially for high-voltage (HV) apparatus in substations at the transmission level [18], [19]. Moreover, in some remote areas, far from any substation or microgrid operated in either grid-connected mode or islanded mode, it is difficult to install and maintain SFMDs due to the lack of facilities and high installation cost. However, it is critical to continually monitor the frequency in such areas in order to maintain reliable and stable operation, especially during

Manuscript received April 28, 2017; revised June 19, 2017; accepted July 6, 2017. Date of publication August 7, 2017; date of current version December 15, 2017. This work was supported in part by the Engineering Research Center Program of the National Science Foundation (NSF) and in part by Department of Energy under NSF Award Number EEC-104187 and in part by the CURENT Industry Partnership Program. *(Corresponding author: Wenxuan Yao.)*

W. Yao, H. Lu, M. J. Till, and W. Gao are with the Department of Electrical Engineering and Computer Science, University of Tennessee, Knoxville, TN 37996 USA (e-mail: wyao3@utk.edu; hlu9@vols.utk.edu; mtill@utk.edu; weigao@utk.edu).

Y. Liu is with the Department of Electrical Engineering and Computer Science, University of Tennessee, Knoxville, TN 37996 USA, and also with Oak Ridge National Laboratory, Oak Ridge, TN 37831 USA (e-mail: liu@utk.edu).

Color versions of one or more of the figures in this paper are available online at http://ieeexplore.ieee.org.

Digital Object Identifier 10.1109/TIE.2017.2736509

disturbance events, e.g., a generation trip or islanding process [39], [40].

Second, since most of the SFMDs utilize GPS signal to align their measurements to coordinated universal time (UTC), SFMDs are vulnerable to reliability deficiencies caused by GPS signal loss and spoofing attacks [20]. Various unpredictable factors such as electromagnetic interference, atmospheric disturbances, inclement weather change changes, man-made GPS signal attacks would lead to the interruption or even failure of satellites signal reception on GPS receivers [21], [22].

Third, current CT- or PT-based SFMDs, e.g., PMUs, are sold as dedicated devices at prices between 6000 and 15 000 USD per unit, depending on the specifications [23]. These high manufacturing costs paired with further installation costs restrict their wide-scale use in power systems [18]. Furthermore, it is difficult to integrate other measurement functions such as power quality monitoring into the specialized processors used in SFMDs.

To overcome the aforementioned issues, one potential solution is to realize the wide area power system frequency measurement with the integration of an efficient, compact, and low-cost wireless electric field sensor (WEFS) in GPS-free embedded mobile systems (MESs). First, according to electromagnetic theory, any electric conductor naturally generates an electric field in the vicinity area [25]. The frequency of this electric field reflects the frequency of the electric conductor while the strength of the electric field is proportional to the voltage level of the electric conductor. If the voltage level of the conductor is sufficiently high (e.g., a 500 kV HV overhead transmission line), the intensity of the electric field at the ground level is significantly stronger than environmental noises [25]. It is, then, feasible to use a WEFS to translate the electric field generated from an HV apparatus into an induced electric signal [26]. Therefore, input signals for frequency measurements can be obtained without a direct physical connection to the system elements. Second, since network time protocol (NTP) can achieve timing accuracy in the order of millisecond level, such precision is sufficient for synchronized frequency measurement. Therefore, it is feasible to use NTP to provide time synchronization signal instead of a GPS signal. An NTP-SFMD has been implemented with the accuracy of 0.2 Hz [24]. To satisfy the synchronized frequency measurement requirement in standards of IEEE C37.118.1 and IEC 61000-4-30, this accuracy must be improved by more than one order to be used in real applications. Third, current widely used MESs, e.g., personal smartphones, can achieve high enough computation speeds to execute real-time measurement algorithms [27]. Implementing the synchronized frequency estimation function on MES will facilitate high-volume deployment with advantages of portability, data visualization, storage, function flexibility, and built-in communication channels.

Traditionally, power grid frequency can be measured using discrete Fourier transform (DFT) based methods with the advantage of high robustness and harmonic immunity. To reduce the influence of picket fence effect and spectral leakage with asynchronous sampling, windowed interpolation DFT algorithms (WIDFT) were used to improve the frequency measurement accuracy [28]–[30]. However, for the conditions requiring high reporting rates, e.g., 10 or 60 Hz and large window size, e.g., 10 cycles, implementations of full DFT calculation required by WIPDFT lead to high computational efforts and bring challenges to meet the real-time requirement for frequency measurement. A recursive DFT (RDFT) phasors calculation method first proposed by Phadke *et al*. [31] was developed with significant reduction on computation. For a six-cycle frequency calculation with 24 samples per cycle, the total computational effort of RDFT is only 4.17% of the conventional DFT. Based on the RDFT in [31], a fast frequency estimation algorithm is used with the accuracy improvement under off-nominal condition via least square estimation and resample calculation. The algorithm is then implemented in the MES for frequency estimation.

Based on these ideas, this paper introduces integration of WEFS into MES (WEFS-MES) for synchronized wireless measurement of the power system frequency. This WEFS-MES can perform wireless frequency measurement in the vicinity of any HV electric conductors. The effectiveness and accuracy of the proposed WEFS-MES are verified via experiments. It can work in tandem with conventional SFMDs to supplement existing wide-area frequency measurement devices.

The rest of this paper is organized as follows: Section II introduces integration of WEFS for signal acquisition. Section III presents an overview of hardware and software design of synchronized frequency measurement on MES. Section IV presents the frequency estimation algorithm on MES. Section IV discusses NTP-based synchronized sampling control technology. Section VI presents the performance evaluation of the proposed system in comparison with other types of SFMDs via experiments. Finally, the conclusion and future work are drawn in Section VII.

II. Technology of the Electric Field Sensor

In this section, the theoretical analysis of electric fields in the vicinity of electric conductors and the integration of WEFS are presented.

A. Electric Field Analysis

The electric field in the vicinity of multiconductor power lines can be evaluated by superimposing the contribution from each conductor. Consider H infinite conductors from A_1 to A_H with the same frequency f_0, the voltage for conductor A_h can be expressed as

$$U_h = Z_h \sin\left(2\pi f_0 t + \varphi_h\right) \tag{1}$$

where φ_h and Z_h are the initial angle and amplitude for conductor A_h. The total electric field $\boldsymbol{E}_T$ of observed point P at the ground panel is the summation from electric field $\boldsymbol{E}_1$ to $\boldsymbol{E}_H$ induced by each conductor as illustrated in Fig. 1. According to the Gauss's law, $\boldsymbol{E}_T$ can be expressed as

$$\boldsymbol{E_T} = \sum_{h=1}^{H} \boldsymbol{d}_n \frac{\lambda_h}{2\pi\varepsilon_0 l_h} \tag{2}$$

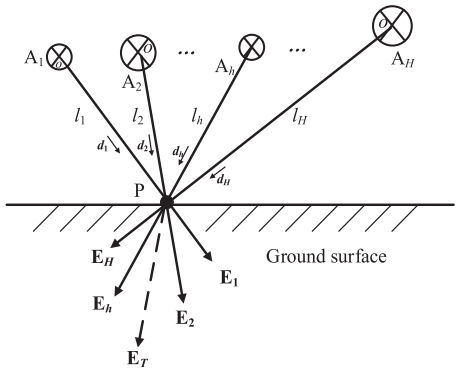

Fig. 1. Electric field calculation of H conductors.

where ε_0 is the permittivity of free space. λ_h is the electric charge density for infinite lines A_h. $\boldsymbol{d}_h$ is the unit direction vector for each conductor which depends on the relative position between the conductor and observed point P. l_h is the distance between the conductor h and the point P. For each conductor, the voltage can be calculated by integrating the electric field along the direction of the radius. Taking conductor A_h as an example, its voltage U_h can be expressed as [32]

$$U_h = \int_{r_h}^{l_h} \frac{\lambda_n}{2\pi\varepsilon_0 r}\, dr = \frac{\lambda_h}{2\pi\varepsilon_0} \ln\left(\frac{l_h}{r_h}\right) \tag{3}$$

where r_h is the radius for the conductor A_h. Rewriting (3), λ_h can be expressed as

$$\lambda_h = \frac{2\pi\varepsilon_0 U_h}{\ln\left(\frac{l_h}{r_h}\right)}. \tag{4}$$

Substituting λ_h into (2), the superposition electric field $\boldsymbol{E_T}$ from $\boldsymbol{E}_1$ to $\boldsymbol{E}_H$ equals to

$$\boldsymbol{E_T} = \sum_{h=1}^{H} \boldsymbol{d}_n \frac{U_h}{\ln\left(\frac{l_h}{r_h}\right) l_h}. \tag{5}$$

Equation (5) exhibits that the strength of the electric field is proportional to the voltage U_h and is inversely proportional to $l_h \ln(l_h)$. The frequency of the electric field $\boldsymbol{E}_T$ is equal to the frequency of each conductor. Therefore, it is feasible to obtain the frequency information of the conductors by measuring the emanated electric field.

B. Integration of WEFS

According to IEEE standard 644-1994 [34], a free-body type sensor is capable of measuring the charging current between the two halves of isolated conductive bodies. Referring to this standard, a WEFS is developed for signal acquisition. The schematic diagram of WEFS is illustrated in Fig. 2. There are two parallel copper regions on the top layer and the bottom layer of the sensor. According to the literature [26], the electric field is capacitively coupled to these regions, inducing an electric potential v_s between these two layers when placing under any HV device, e.g., the transmission line right-of-way (ROW). A voltage follower is used to achieve high input impedance for the

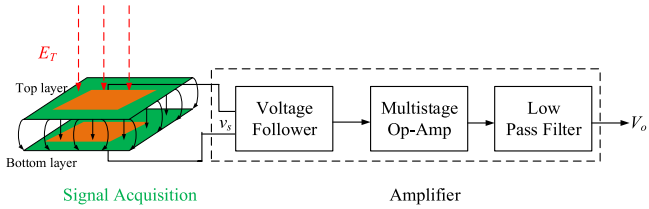

Fig. 2. Schematic diagram of WEFS.

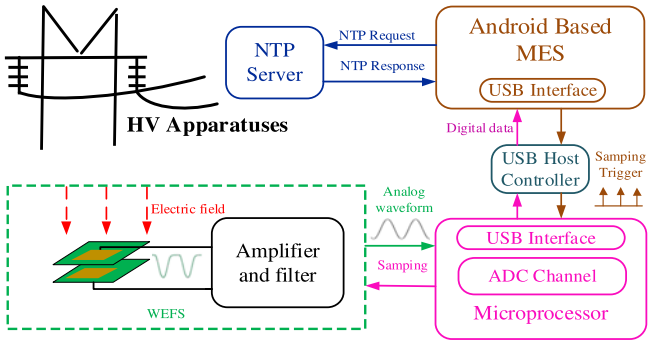

Fig. 3. Hardware design of the WEFS-MES.

input signal v_s. The output voltage is then amplified by a multistage operational amplifier to fit the range of an A/D converter. The amplified voltage signal is filtered by a low-pass filter to cut high-frequency components and then fed to the input of the A/D converter.

Larger dimensions of isolated conductive layers will help to avoid the edge effect [34]. On the other hand, to make the measurement device portable, the size of WEFS needs to be as small as possible. To balance the above tradeoff, the dimension of the WEFS is 5.05 cm × 3.05 cm × 0.16 cm. Furthermore, to enhance the flexibility of the WEFS, the gain ratio of the amplifier is adjustable to accommodate different signal strengths.

III. Synchronized Frequency Measurement on MES

In this section, the overview of hardware and software designs for synchronized frequency measurement using MES is presented.

A. Overview of Hardware Design

The hardware design is shown in Fig. 3. The hardware of the MES is composed of WEFS, a microprocessor-based AD sampling module, and an Android-based MES. The complete system can be assembled within 300 USD.

In the prototype development, an Android-based Nexus S equipped with a 512 MB memory and 1 GHz CPU clock is used as the MES for frequency estimation. The WEFS, which replaces the traditional PT and CT, is used to acquire input signal from HV electric conductors. The induced signals are amplified and filtered by a low-pass filter with a cut-off frequency of 900 Hz, rejecting high-frequency noise and harmonic inference. An Arduino board with a microprocessor ATmega328 is used to sample the analog signal from the WEFS at a sampling

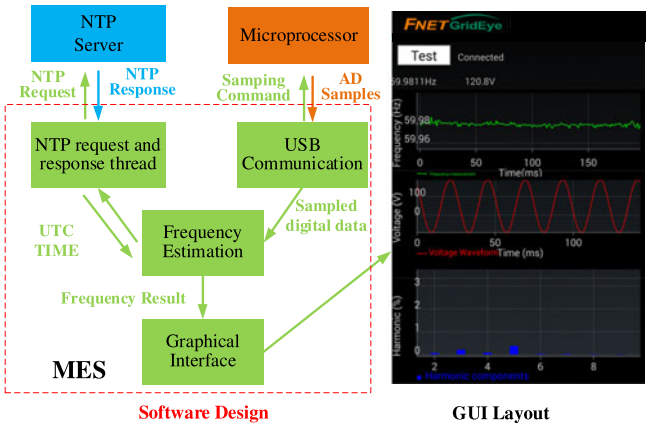

Fig. 4. Illustration of software design and the GUI layout on MES.

frequency 1440 Hz (24 sample per cycle for 60 Hz power system) and send the raw digital data to the MES for data processing. The bidirectional data communication between the Arduino Uno board and the MES is realized by the USB host controller IC MAX3421E. The ATmega328 communicates with the USB host controller via a serial peripheral interface bus and behaves as USB master. The MES, as USB slave, sends sampling commands to the microprocessor and receives sampled digital signals. The MES sends requests to the NTP server for NTP time synchronization via network access. Real-time information including frequency and the waveform is displayed on the screen. The measurements with their UTC time index are stored in a database on the MES and then uploaded to the data server.

B. Software Design on MES

The software design and its graphic user interface (GUI) layout developed for an Android-based MES are illustrated in Fig. 4.

The computationally intensive tasks including frequency estimation and NTP request and response are executed in a separate thread instead of placing in the main thread to increase the efficiency. The application mainly includes the USB communication thread, the NTP request and response thread, the frequency estimation thread, and the GUI thread. The USB communication thread receives digitally sampled data from the microprocessor. Once six cycles' samples are received by the MES from the USB connection, the estimation thread calculates the real-time frequency. The USB communication thread continuously monitors the USB accessory connection status and is configured as "plug-and-play" mode, which means when the MES is connected to the USB host controller with a "handshake," the whole application will run automatically. The UTC time is obtained by a request to the NTP server from the NTP request and response thread. Then, received NTP time is used for local clock calibration and synchronized sampling control. Finally, the frequency measurement results and real-time waveform are visually displayed at the MES screen via executing the GUI thread.

IV. Frequency Estimation Algorithm

A. Recursive DFT-Based Frequency Estimation

Given N data points of signal $\{x_i\}$ per cycle $i \in [1\ N]$, the phasor of the fundamental frequency components is

$$\bar{X}_{(1)} = \frac{1}{\sqrt{2}}\left(X_1^c - j \cdot X_1^s\right) \tag{6}$$

where j is the imaginary unit. $X_{(1)}^c$ and $X_{(1)}^s$ can be expressed as

$$X_{(1)}^c = \frac{2}{N}\sum_{i=1}^{N} x_i \cos\left(\frac{2\pi i}{N}\right) \tag{7}$$

$$X_{(1)}^s = \frac{2}{N}\sum_{i=1}^{N} x_i \sin\left(\frac{2\pi i}{N}\right). \tag{8}$$

After the one cycle initialization, the successive $\bar{X}_{i+1}$ phasor for incoming data x_{i+1} can be recursively computed from $\bar{X}_i$ and the data points x_{i+1} and x_{i+1-N} as [36]

$$\bar{X}_{(i+1)} = \bar{X}_i + j\frac{\sqrt{2}}{N}\left(x_{i+1} - x_{i+1-N}\right)\exp\left(-j\frac{2\pi i}{N}\right). \tag{9}$$

Thus, the new real and imaginary components can be expressed as

$$X_{(i+1)}^c = X_i^c + \frac{2}{N}\left(x_{i+1} - x_{i+1-N}\right)\cos\left(\frac{2\pi i}{N}\right) \tag{10}$$

$$X_{(i+1)}^s = X_i^s + \frac{2}{N}\left(x_{i+1} - x_{i+1-N}\right)\sin\left(\frac{2\pi i}{N}\right). \tag{11}$$

For the numbers of 24 and 48 samples per cycle, the computation complexities for RDFT are only 4.17% and 2.18% of conventional DFT, which will greatly reduce the overload of CPU in embedded systems for a real-time signal analysis.

The amplitude P_i and angle θ_i of the ith phasor can be obtained by

$$P_i = \left(X_{(i)}^{c\ 2} + X_{(i)}^{s\ 2}\right)^{\frac{1}{2}} \tag{12}$$

$$\theta_i = \tan^{-1}\left(\frac{-X_{(i)}^s}{X_{(i)}^c}\right). \tag{13}$$

The DFT angle measurement can be obtained by (13). The frequency measurement can be estimated by the rate change of angles. A least-square method (LSM) is used to calculate the rate of angle change. When the frequency is constant, the angle varies following a linear function. It is assumed that real power grid frequency generally keeps constant in the DFT windows (0.1 s when $N = 144$) in the standards [16], [17] and for most of synchronized frequency measurement based applications, e.g., islanding detection [39] and generation trip detection [40], 0.1 s resolution is sufficiently high to capture the characteristic of frequency during disturbance events. A second-order polynomial function is sufficient to represent the angle with the sample index, which can be expressed as

$$\theta_{(v)} = \alpha_0 + \alpha_1 v + \alpha_2 v^2 \tag{14}$$

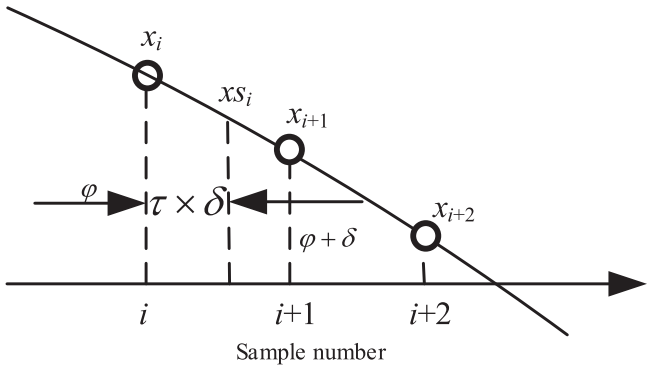

Fig. 5. Illustration of the resampling procedure.

where v is an index for the angles. α_0, α_1, and α_2 are the coefficients for quadratic function. Converting (14) into matrix form, it can be expressed as

$$\boldsymbol{\theta} = \boldsymbol{V}\boldsymbol{\alpha} \tag{15}$$

where angle matrix $\boldsymbol{\theta} = [\theta_1 \ \cdots \theta_v \ \cdots \theta_V \ ]^{\mathrm{T}}$, coefficient matrix $\boldsymbol{\alpha} = [\alpha_0 \ \ \alpha_1 \ \ \alpha_2]^{\mathrm{T}}$, and $\boldsymbol{V}$ is a constant valued matrix satisfying

$$\boldsymbol{V} = \begin{bmatrix} 1 & 1 & 1 \\ \vdots & \vdots & \vdots \\ 1 & V & V^2 \end{bmatrix} \tag{16}$$

where V is the total number of the angles used for frequency calculation.

As the matrices $\boldsymbol{V}$ and $\boldsymbol{\theta}$ are both known in (15), the coefficient $\boldsymbol{\alpha}$ can be obtained by pseudo-inverse computation as

$$\boldsymbol{\alpha} = \left[\boldsymbol{V}^{\boldsymbol{T}}\boldsymbol{V}\right]^{-1}\boldsymbol{V}^{\boldsymbol{T}}\boldsymbol{\theta}. \tag{17}$$

Therefore, the first estimated frequency deviation $\Delta f_{(1)}$ can be obtained as

$$\Delta f_{(1)} = \frac{1}{2\pi} N f_0 \left(\alpha_1 + 2\alpha_2 v\right) \tag{18}$$

where f_0 is the nominal frequency (e.g., 60 Hz). Thus, the first measured frequency can be obtained by

$$f_1 = f_0 + \Delta f_{(1)}. \tag{19}$$

B. Resample Procedure

To enhance the performance of frequency measurement under off-nominal condition, f_1 will be regarded as the nominal frequency of the resampling process. Since the sampling rate of ADC in MES is fixed, in order to keep constant sampling number per cycle that angle increments at the speed of $2\pi/N$, the input signal is resampled via interpolation as illustrated in Fig. 5. Defining the origin samples, x_i and x_{i+1} are

$$x_i = \mathrm{AP}\sin\varphi \tag{20}$$

$$x_{i+1} = \mathrm{AP}\sin\left(\varphi + \delta\right) \tag{21}$$

where AP is the amplitude of the input signal; and φ is an instantaneous angle for x_i. δ is angle difference between two samples at the frequency f_1, satisfying $\delta = 2\pi f_1/(N f_0)$. When

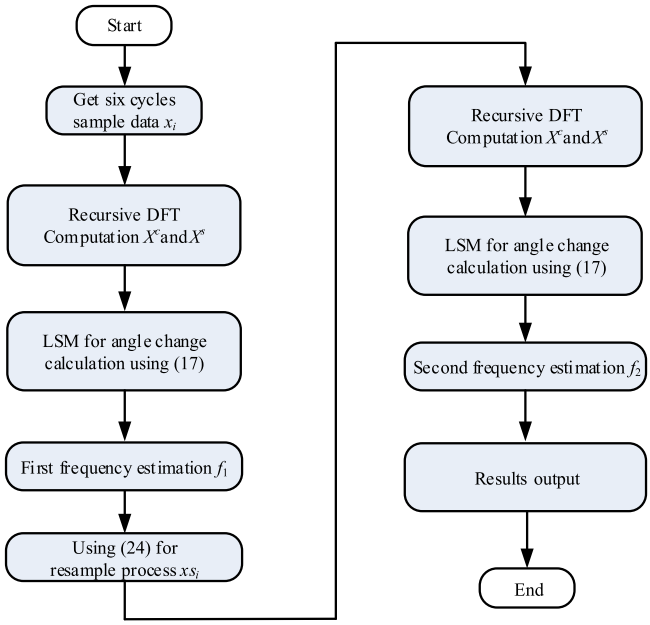

Fig. 6. Workflow of the frequency estimation algorithm.

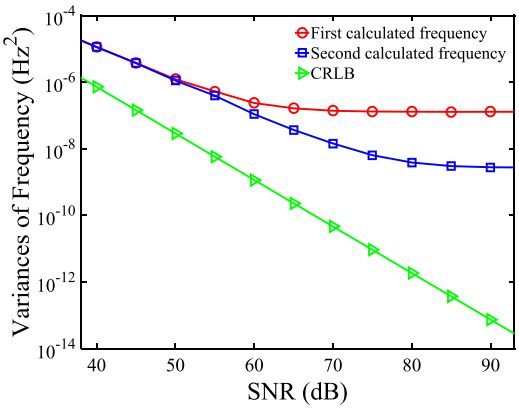

Fig. 7. Variances of frequency measurement when $\Delta f = 0.15$ Hz.

$f_1 = f_0$, δ is equal to $2\pi/N$. To correct δ to be $2\pi/N$ when $f_1 \neq f_0$, a resample process is performed.

Assuming the resample point xs_i is between samples x_i and x_{i+1}, the value of the xs_i can be expressed as

$$xs_i = \mathrm{AP}\sin\left(\varphi + \tau\delta\right) \tag{22}$$

where τ is the fractional number between 0 and 1 representing relative distance of resampled point xs_i to x_i and x_{i+1}, which can be obtained by

$$\tau = i \times \frac{f_0}{f_1} - \mathrm{Fl}\left(i \times \frac{f_0}{f_1}\right) \tag{23}$$

where Fl() denotes the function that rounds a noninteger down to the nearest integer.

TABLE I
RMSE OF FREQUENCY MEASUREMENT (HZ) WITH WHITE NOISE

Δf (Hz)	First calculated frequency f_1			Second calculated frequency f_2		
	SNR			SNR		
	40 dB	60 dB	80 dB	40 dB	60 dB	80 dB
–0.20	2.21×10^{-2}	4.93×10^{-3}	9.83×10^{-4}	1.48×10^{-2}	2.96×10^{-3}	4.95×10^{-4}
–0.10	9.02×10^{-3}	3.95×10^{-3}	4.89×10^{-4}	5.41×10^{-3}	1.82×10^{-3}	4.11×10^{-4}
–0.05	8.79×10^{-3}	3.21×10^{-3}	4.41×10^{-4}	7.97×10^{-3}	1.18×10^{-3}	2.01×10^{-4}
0.00	7.81×10^{-3}	8.90×10^{-4}	1.35×10^{-4}	5.89×10^{-3}	8.87×10^{-4}	1.42×10^{-4}
0.05	8.25×10^{-3}	1.48×10^{-3}	4.24×10^{-4}	8.01×10^{-3}	1.26×10^{-3}	1.98×10^{-4}
0.10	9.63×10^{-3}	1.51×10^{-3}	5.31×10^{-4}	4.68×10^{-3}	1.31×10^{-4}	2.54×10^{-4}
0.20	2.47×10^{-2}	1.97×10^{-3}	8.21×10^{-4}	2.98×10^{-2}	1.47×10^{-4}	6.75×10^{-4}

Expanding (20)–(22) using trigonometric identifies and substituting (20), (21) into (22), xs_i can be calculated as

$$xs_i = x_i \cos \tau\delta + (x_{i+1} - x_i \cos \delta) \frac{\sin \tau\delta}{\sin \delta} \tag{24}$$

Applying the above-mentioned RDFT algorithm on resample data $\{xs_i\}$, the second calculated frequency measurement f_2 is

$$f_2 = f_1 + \Delta f_2 \tag{25}$$

where Δf_2 is the second estimated frequency deviation. f_2 will be output as the final calculated frequency in the MES.

C. Complete Process for Frequency Estimation

By using the RDFT and resample method discussed above, the real-time frequency can be measured with low CPU workload on the MES. Once 144 samples (0.1 s) are received, the frequency estimation algorithm is performed. The flowchart of the frequency estimation algorithm is presented in Fig. 6 and can be outlined with the following steps:

Step 1: Apply RDFT and obtain angle matrix θ.
Step 2: Calculate the rate of change of angle using LSM from (17) and obtain the measured frequency from (19).
Step 3: Use the first measured frequency f_1 as the nominal frequency for resampling and obtain resample data xs using (23) and (24).
Step 4: Repeat *step 1* and *step 2* and obtain the second frequency estimation f_2.

D. Accuracy of the Frequency Estimation Algorithm

To evaluate the accuracy of the frequency estimation algorithm, simulations are conducted using sinewave signal distorted by white noise with different SNR, where sampling rate is 1440 Hz. The SNR changes from 35 to 95 dB and for each value of SNR 1000 runs have been performed to evaluate the statistical properties of the algorithm. The frequency of the input signal is 60.15 Hz ($\Delta f = 0.15$ Hz). The Cramer–Rao lower bound (CRLB) is considered to provide a quantitative benchmark of frequency measurement error as shown in Fig. 7. In this semilog plot, it can be seen that the second calculated frequency is closer to the CRLB, implying that the resample process improves the accuracy under the off-nominal condition. Table I lists root mean square errors (RMSE) for the simulated signals whose fundamental frequency deviation Δf and superposed noise change from –0.2 to +0.2 Hz and 40–80 dB, respectively. The RMSE of f_2 is smaller than 2×10^{-3} Hz when the SNR is larger than 60 dB. For the input signal with $\Delta f = +0.2$ Hz and SNR = 60 dB, the error of f_2 with 1.47×10^{-3} Hz is lower than f_1 with 1.97×10^{-3} Hz. Considering that the SNR of actual power grid signal is from 60 to 80 dB [37], the error of 1.47×10^{-3} Hz under the condition of 60 dB complies with requirements on both IEC61000-4-30 and IEEE C37.118.1 where error should be smaller than 1×10^{-2} and 5×10^{-3} Hz, respectively, demonstrating that the proposed algorithm is suitable for real power system frequency estimation.

TABLE II
RMSE OF FREQUENCY MEASUREMENT (HZ) WITH INTERFERENCE

Interference Type	Harmonic			
	2nd order	3rd order	5td order	7td order
RMSE	5.11×10^{-5}	5.13×10^{-5}	5.14×10^{-5}	5.19×10^{-5}
Interference Type	Interharmonic		Modulation	
	95 Hz	110 Hz	PAM	AM
RMSE	3.72×10^{-3}	4.68×10^{-3}	9.19×10^{-3}	5.24×10^{-4}

The performances of the estimation algorithm are further evaluated with signals distorted by harmonic, interharmonic, amplitude modulation (AM), and phase angle modulation (PAM). The simulated signal is constructed based on the recommendation in the IEEE standard C37.118.1 [16]. The impact of second, third, fifth, and seventh harmonic order is analyzed. The harmonic amplitude is 10% of the fundamental component, which is the worst condition stated in the standard. For the two interharmonic impact tests, the signals are distorted with 10% 95 and 110 Hz interharmonic component. For modulation test, modulation factor and modulation frequency are 10% and 2 Hz for both AM and PAM. The fundamental frequency is 60.02 Hz, and 1000 runs have been performed for each case. The results are listed in Table II. It can be seen that the impact of harmonic and PAM is considerably smaller than interharmonic and AM. The RSME under the conditions harmonic distortion is in the order of 10^{-5} Hz, which is negligible considering 5×10^{-3} Hz

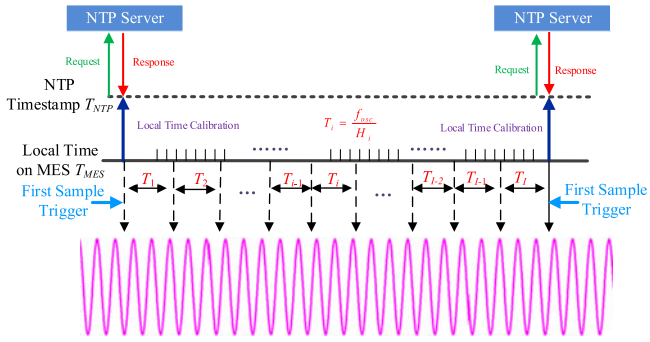

Fig. 8. NTP-based synchronized sampling control technology.

limit in [16]. Interharmonic and PAM cause larger estimation error. The RMSE of 9.19×10^{-3} and 5.24×10^{-4} Hz for PAM and AM, respectively, sufficiently satisfies the standard which requires frequency error smaller than 1×10^{-2} Hz under the modulation conditions.

V. Synchronized Sampling Control Technology

One critical factor of frequency measurement on MES is to develop a synchronized sampling technology. Unlike in traditional SFMDs that utilize GPS signals for time synchronization, the MES uses NTP for synchronized sampling control. In this section, the synchronized sampling technology on MES including NTP-based local time synchronization and sampling interval control are presented.

A. MES Local Time Synchronization Via NTP

Ideally the local time stamp on MES should be identical with NTP time stamp. However, the local time of an MES is likely to drift due to the variation of the operation frequency of an oscillator influenced by various factors including the change of environmental temperature and aging. Therefore, NTP is used for local time synchronization on MES as illustrated in Fig. 8. Defining that the synchronization cycle is configured to be m seconds, a timer on MES is used to trigger the first sample of each synchronization cycle via the USB connection. To eliminate the accumulative timing error due to the local time drifts, the received NTP time stamp, acted as a reference, is continuously compared with the local time stamp. When the difference between the latest NTP time stamps T'_{NTP} and the local time stamp T'_{MES} is larger than threshold of NTP time error ε satisfying

$$|T'_{\text{NTP}} - T'_{\text{MES}}| > \varepsilon \tag{26}$$

the control parameter (CP) for the local timer on MES will be adjusted as follows:

$$\text{CP} = m \cdot \frac{T_{\text{MES}} - T'_{\text{MES}}}{T_{\text{NTP}} - T'_{\text{NTP}}} \tag{27}$$

where T_{NTP} and T_{MES} are the previous NTP and local time stamps, respectively. Meanwhile, the local time is updated from T'_{MES} to T'_{NTP} and is used as a time stamp to tag each frequency measurement.

B. Sampling Interval Control

The sampling interval inside the m-seconds synchronization cycle, shown in Fig. 8, is controlled only by a timer period register (TPR) in the microprocessor. The value of TPR (VTPR) determines the number of pulses to count for triggering a sampling command, which can be expressed as

$$\text{VTPR} = \frac{f_{\text{osc}}}{f_s} \tag{28}$$

where f_{osc} is the operation frequency of the oscillator (e.g., 16 MHz for ATmega328), and f_s is the desirable sampling rate of 1440 Hz. A timer counter register (TCR) is used to count the clock pulses and an interrupt will be triggered to send a sampling command when TCR reaches VTPR. Ideally, the TPR is set to be exactly equal to VTPR. However, in implementation, TPR has to be configured as an integer number while VTPR is usually a fractional number according to (28), e.g., $f_{\text{osc}} = 16$ MHz and $f_s = 1440$ Hz. The integer restriction of TPR and its conflict to the fractional number VTPR will inevitably introduce a division remainder and consequently degrade the sampling accuracy. Assuming VTPR_A and VTPR_B are the nearest integers around VTPR, satisfying $\text{VTP}R_A + 1 = \text{VTPR}_B$, a sampling time error will be introduced whichever VTPR_A or VTPR_B is selected. To reduce the sampling error, VTPR_A and VTPR_B can be alternately set as TPR to approach the real VTPR [35]. For the ith sample in an m-second synchronization cycle, either VTPR_A or VTPR_B is selected to control the sampling intervals determined by the following criterion:

$$\text{VTPR}_i = \begin{cases} \text{VTPR}_A & \left(\text{if } \frac{G_i}{i} \geq \text{FP}\right) \\ \text{VTPR}_B & \left(\text{if } \frac{G_i}{i} < \text{FP}\right) \end{cases} \tag{29}$$

where FP is the fractional part of VTPR in (28). G_i is a control variable to count the number of times VTPR_B has been selected, which can be expressed as

$$G_i = \begin{cases} G_{i-1} + 1 & \text{when } \text{VTPR}_B \text{ is selected} \\ G_{i-1} & \text{when } \text{VTPR}_A \text{ is selected} \\ 0 & \text{when } i = 0 \end{cases} \tag{30}$$

VTPR_A and VTPR_B are selected proportionally according to (29) and (30), where the ratio of VTPR_A and VTPR_B is only determined by the FP. This variable sampling control can greatly reduce the sampling time error caused by the division remainder. In order to resolve the timing error between VTPR_A and VTPR_B smoothly, the use of both VTPR_A and VTPR_B is distributed across m seconds.

VI. Performance Evaluation

In order to examine and verify the effectiveness and accuracy of proposed system, experiments are conducted with input signals from both a signal generator and the real power grid. The collected frequency measurements are sent to the FNET/GridEye server for performance evaluation. A comparison

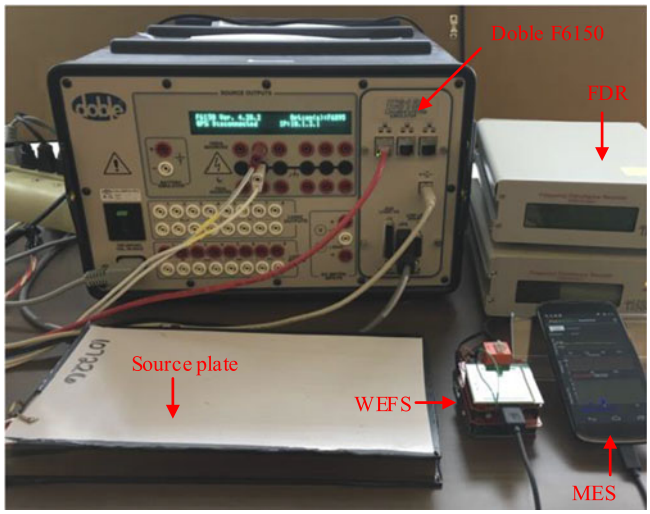

Fig. 9. Experiment setup.

between different kinds of SFMDs including PT-based FDR (PT-FDR), WEFS-based FDR (WEFS-FDR), PT-based MES (PT-MES), and WEFS-MES is conducted. In order to obtain a fair comparison for the wireless sensor and MES, these four devices are set up with the same frequency estimation algorithm and sampling control method given in Sections VI and V, respectively.

A. Experiment Setup

The strength of an electric field in the ROW of 500 kV transmission line corridors is generally in the range of 0.3–10 kV/m [33], [38]. Therefore, in the experiments, to simulate the condition at the edge of a transmission line ROW, a 5 kV/m electric field is generated by two parallel copper plates, referred as source plates. The length and width of the source plates are 30.48 cm and 15.25 cm, respectively. The distance between the two source plates is 2.4 cm.

In the first experiment, a Doble F6150 power system simulator is used to generate ac power to the source plates. By varying the output frequency of the Doble F6150, the performance of WEFS-MES and WEFS-FDR can be evaluated under off-nominal conditions. For the PT-MES and PT-FDR, the input signal is directly obtained from Doble F6150. The experimental setup for WEFS-MES is shown in Fig. 9.

In the second experiment, the source plates are connected to an ambient real-world power grid signal. For the WEFS-MES and WEFS-MES, the input signal is wirelessly captured in WEFS and is then sent to the MES for frequency estimation. For the PT-MES and PT-FDR, the input signals are directly obtained from a power grid.

PT-FDR and WEFS-FDR are required to receive stable GPS signals while PT-MES and WEFS-MES are connected with NTP server throughout the test for time synchronization. The measurements are time-stamped with NTP time index in the MESs and GPS time index in FDRs. All measurement data from these four devices are transmitted to the FNET/GridEye server for comparison.

TABLE III
RMSE OF FREQUENCY MEASUREMENT (HZ)

Input Frequency(Hz)	PT-FDR	WEFS-FDR	PT-MES	WEFS-MES
59.90	7.92×10^{-4}	9.46×10^{-4}	9.42×10^{-4}	1.89×10^{-3}
59.98	3.78×10^{-4}	8.31×10^{-4}	8.23×10^{-4}	9.97×10^{-4}
60.00	2.04×10^{-4}	6.36×10^{-4}	4.58×10^{-4}	7.23×10^{-4}
60.02	4.87×10^{-4}	9.98×10^{-4}	1.51×10^{-3}	2.05×10^{-3}
60.10	8.28×10^{-4}	1.02×10^{-3}	1.95×10^{-3}	2.37×10^{-3}

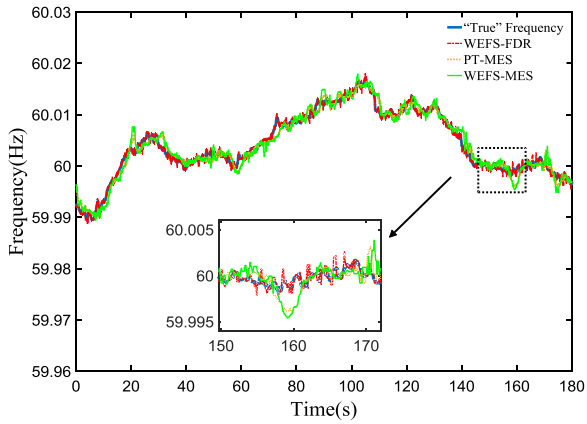

Fig. 10. Frequency measurement comparison with power grid signal.

B. Experiment Result

By using an RDFT algorithm for complexity reduction, this frequency measurement application only consumes less than 8% of the CPU usage, which will not significantly impact other functions of the MES.

For the first experiment using signals from Doble F6150, the fundamental frequency changes from 59.90 to 60.10 Hz. The RMSE of frequency measurement under different input frequency is listed in Table III. The RMSE of WEFS-FDR is less than 1.02×10^{-3} Hz, compared to 8.28×10^{-4} Hz for the PT-FDR, verifying the effectiveness of WEFS for signal acquisition. The RMSE for WEFS-MES is 2.37×10^{-3} Hz, which is close to the result of WEFS-FDR 1.02×10^{-3} Hz. This result demonstrates that the MES is able to achieve almost the same accuracy in frequency measurement as the FDR with fundamental frequency variation. According to IEC61000-4-30, the standard for power quality monitoring of Class A, the measurement uncertainty shall not exceed 0.01 Hz. From Table III, the RMSE of WEFS-MES is smaller than 2.37 MHz, which is sufficient to comply with this requirement.

For the second experiment using an ambient real-world power grid signal, the measurement results for 180 s are plotted in Fig. 10. Unlike experiments using the signal from a signal generator, the real true frequency of real power grid signal is unknown. To make the comparison, the measurement of PT-FDR, which can achieve the accuracy of 5×10^{-4} Hz [13], is used as "true" frequency. It can be seen in Fig. 10 that the WEFS-MES has the ability to synchronously capture the trends of power grid frequency over time. The experiment results indicate that

TABLE IV
COMPARISON OF FREQUENCY MEASUREMENT ERROR (HZ)

	WEFS-FDR	PT-MES	WEFS-MES
RMSE	5.34×10^{-4}	2.31×10^{-3}	3.47×10^{-3}
MAXE	1.05×10^{-3}	4.95×10^{-3}	5.17×10^{-3}

TABLE V
COMPARISON WITH OTHER KINDS OF SFMDS

SFMDs	PMU	FDR	PT-MES	WEFS-FDR	WEFS-MES
Accuracy (Hz)	1.01×10^{-4}	2.04×10^{-4}	6.36×10^{-4}	4.58×10^{-4}	7.23×10^{-4}
Portability	N	N	Y	Y	Y
HV Meas.	Y	N	N	Y	Y
GPS Reliance	Y	Y	N	Y	N
Inst. Effort	High	Median	Low	Median	Low
Approx. Cost ($)	6000	1000	500	800	300

the proposed system with advantages of low cost and convenience has high accuracy in the power system frequency measurement as other SFMDs. The RMSE and maximum absolute error (MAXE) are listed in Table IV, the RMSE of WEFS-MES and PT-MES is 3.47×10^{-3} and 2.31×10^{-3} Hz, verifying that the WEFS can measure accuracy as the PT. It is mentioned that the SNR of actual power grid signal is from 60 to 80 dB, the RMSE of 3.47×10^{-3} Hz for WEFS-MES in Table IV is close to 1.82×10^{-3} Hz for SNR $= 60$ dB and $\Delta f = -0.1$ Hz in Table I, which shows a good agreement between simulation and experiments.

C. Comparison With Other SFMD

Table V lists the comparison of the proposed system with other types of SFMDs in the aspects of accuracy, portability, HV measurement capability, GPS reliance, Installation (Inst.) effort, and cost. Although the accuracy level of WEFS-MES is slightly lower than other SFMDs, WEFS-MES has the remarkable advantages for low cost and minimal installation efforts, facilitating wide application of future frequency measurement in transmission line network. Unlike traditional SFMDs, the WEFS-MES is portable and flexible for HV frequency measurement. Furthermore, the GPS reliance in conventional PMU and FDR is eliminated by utilizing NTP-based synchronization in MES, which will greatly broaden the SFMDs family.

VII. CONCLUSION AND FUTURE WORK

This paper presented a synchronized wireless measurement of wide area power system frequency using MES integrated with WEFS. Experiments verified the effectiveness and accuracy of the proposed systems. Compared with traditional SFMDs, the proposed WEFS-MES has the advantages of portability and flexibility. Furthermore, it significantly reduced manufacturing and installation costs, which will facilitate large-scale deployment of a wide area frequency monitoring system. The main contribution of this paper includes

1) A WEFS was used to replace traditional PTs and CTs for signal acquisition, which significantly reduced manufacturing and installation costs and increased the flexibility of frequency measurement.
2) An RDFT-based estimation algorithm was used in MES for real-time frequency calculation with low computational overload. The performance of the algorithm was evaluated via simulation and experiment.
3) The NTP-based synchronized sampling control method was proposed and implemented, compensating the sampling time error caused by local time drift and eliminating the GPS reliance.

Further work includes improving the NTP time synchronization accuracy by latency calibration, increasing the reliability of WEFS, system simplification, field tests, and integrating more functionality such as phasor measurement and power quality monitoring.

REFERENCES

[1] H. Wen, S. Guo, Z. Teng, F. Li, and Y. Yang, "Frequency estimation of distorted and noisy signals in power systems by FFT-based approach," *IEEE Trans. Power Syst.*, vol. 29, no. 2, pp. 765–774, Mar. 2014.

[2] C. J. Ramos, A. P. Martins, and A. S. Carvalho, "Frequency and phase-angle estimation using ordinary least squares," *IEEE Trans. Ind. Electron.*, vol. 62, no. 9, pp. 5677–5688, Sep. 2015.

[3] L. Wang, Q. Jiang, L. Hong, C. Zhang, and Y. Wei, "A novel phase-locked loop based on frequency detector and initial phase-angle detector," *IEEE Trans. Power Electron.*, vol. 28, no. 10, pp. 4538–4549, Oct. 2013.

[4] M. S. Reza, M. Ciobotaru, and V. G. Agelidis, "A modified demodulation technique for single-phase grid voltage fundamental parameter estimation," *IEEE Trans. Ind. Electron.*, vol. 62, no. 6, pp. 3705–3713, Jun. 2015.

[5] C. I. Chen, "Design of measurement system based on signal reconstruction for analysis and protection of distributed generations," *IEEE Trans. Ind. Electron.*, vol. 60, no. 4, pp. 1652–1658, Apr. 2013.

[6] M. D. Kusljevic, J. J. Tomic, and L. D. Jovanovic, "Frequency estimation of three-phase power system using weighted-least-square algorithm and adaptive FIR filtering," *IEEE Trans. Instrum. Meas.*, vol. 59, no. 2, pp. 322–329, Feb. 2010.

[7] A. Radonjic, P. Sovilj, and V. Vujicic, "Stochastic measurement of power grid frequency using a two-bit A/D converter," *IEEE Trans. Instrum. Meas.*, vol. 63, no. 1, pp. 56–62, Jan. 2014.

[8] V. Terzija, D. Cai, V. Stanojevic, and G. Strbac, "Frequency and power components estimation from instantaneous power signal," *IEEE Trans. Instrum. Meas.*, vol. 60, no. 11, pp. 3640–3649, Nov. 2011.

[9] F. Zhang, L. Cheng, X. Li, Y. Sun, W. Gao, and W. Zhao, "Application of a real-time data compression and adapted protocol technique for WAMS," *IEEE Trans. Power Syst.*, vol. 30, no. 2, pp. 653–662, Mar. 2015.

[10] A. Moreno-Munoz, V. Pallares-Lopez, J. J. Gonzalez de la Rosa, R. Real-Calvo, M. Gonzalez-Redondo, and I. M. Moreno-Garcia, "Embedding synchronized measurement technology for smart grid development," *IEEE Trans. Ind. Informat.*, vol. 9, no. 1, pp. 52–61, Feb. 2013.

[11] W. Yao *et al.*, "Source location identification of distribution-level electric network frequency signals at multiple geographic scales," *IEEE Access*, vol. 5, pp. 11166–11175, 2017.

[12] A. G. Phadke, J. S. Thorp, R. F. Nuqui, and M. Zhou, "Recent developments in state estimation with phasor measurements," in *Proc. IEEE/PES Power Syst. Conf. Expo.*, Seattle, WA, 2009, pp. 1–7.

[13] Y. Liu *et al.*, "Wide-area-measurement system development at the distribution level: An FNET/GridEye example," *IEEE Trans. Power Del.*, vol. 31, no. 2, pp. 721–731, Apr. 2016.

[14] J. Chai *et al.*, "Wide-area measurement data analytics using FNET/GridEye: A review," in *Proc. Power Syst. Comput. Conf.*, Genoa, 2016, pp. 1–6.

[15] Y. Liu *et al.*, "Recent developments of FNET/GridEye—A situational awareness tool for smart grid," *CSEE J. Power Energy Syst.*, vol. 2, no. 3, pp. 19–27, Sep. 2016.

[16] *IEEE Standard for Synchrophasors for Power System*, IEEE Std. C37.118.1, 2006.
[17] *Testing and Measurement Techniques - Power Quality Measurement Methods*, IEC Std. 61000-4-30, 2015.
[18] W. Yao, Y. Zhang, Y. Liu, M. J. Till, and Y. Liu, "Pioneer design of non-contact synchronized measurement devices using electric and magnetic field sensors," *IEEE Trans. Smart Grid*, 2017, to be published. DOI: 10.1109/TSG.2017.2692726.
[19] Y. Zhang, W. Yao, J. Culliss, G. Zhang, Z. Teng, and Y. Liu, "Electrical field based wireless devices for contactless power gird phasor measurement," in *Proc. IEEE PES Gen. Meeting*, 2014, pp. 1–5.
[20] W. Yao *et al.*, "Impact of GPS signal loss and its mitigation in power system synchronized measurement devices," *IEEE Trans. Smart Grid*, 2017, to be published. DOI: 10.1109/TSG.2016.2580002.
[21] Z. Zhang, S. Gong, A. D. Dimitrovski, and H. Li, "Time synchronization attack in smart grid: Impact and analysis," *IEEE Trans. Smart Grid*, vol. 4, no. 1, pp. 87–98, Mar. 2013.
[22] L. Zhan, Y. Liu, W. Yao, J. Zhao, and Y. Liu, "Utilization of chip scale atomic clock for synchrophasor measurements," *IEEE Trans. Power Del.*, vol. 31, no. 5, pp. 2299–2300, Oct. 2016.
[23] D. M. Laverty, R. J. Best, P. Brogan, I. Al Khatib, L. Vanfretti, and D. J. Morrow, "The OpenPMU platform for open-source phasor measurements," *IEEE Trans. Instrum. Meas.*, vol. 62, no. 4, pp. 701–709, Apr. 2013.
[24] K. A. Salunkhe and A. Kulkarni, "A wide area synchronized frequency measurement system using network time protocol," in *Proc. 16th Natl. Power Syst. Conf.*, 2010, pp. 266–271.
[25] G. Wijeweera, B. Bahreyni, C. Shafai, A. Rajapakse, and D. R. Swatek, "Micromachined electric-field sensor to measure ac and dc fields in power systems," *IEEE Trans. Power Del.*, vol. 24, no. 3, pp. 988–995, Jul. 2009.
[26] M. Yazdani, D. J. Thomson, and B. Kordi, "Passive wireless sensor for measuring ac electric field in the vicinity of high-voltage apparatus," *IEEE Trans. Ind. Electron.*, vol. 63, no. 7, pp. 4432–4441, Jul. 2016.
[27] Y. Liu, W Yao, L. Zhan, H. Lu, and W. Gao, "Mobile electric field sensor based phasor measurement unit for monitoring an electric power grid," U.S. Patent 20 160 025 785, Jan. 28, 2016.
[28] H. Wen, C. Li, and W. Yao, "Power system frequency estimation of sine-wave corrupted with noise by windowed three-point interpolated DFT," *IEEE Trans. Smart Grid*, 2017, to be published. DOI: 10.1109/TSG.2017.2682098.
[29] D. Belega and D. Dallet, "Multifrequency signal analysis by Interpolated DFT method with maximum sidelobe decay windows," *Measurement*, vol. 42, pp. 420–426, 2009.
[30] J. Borkowski, D. Kania, and J. Mroczka, "Interpolated-DFT-based fast and accurate frequency estimation for the control of power," *IEEE Trans. Ind. Electron.*, vol. 61, no. 12, pp. 7026–7034, Dec. 2014.
[31] A. G. Phadke, J. S. Thorp, and M. G. Adamiak, "A new measurement technique for tracking voltage phasors, local system frequency, and rate of change of frequency," *IEEE Trans. Power App. Syst.*, vol. PAS-102, no. 5, pp. 1025–1038, May 1983.
[32] G. S. N. Raju, *Electromagnetic Field Theory and Transmission Lines*. India: Pearson, Jun. 2006.
[33] *Transmission Line Reference Book, 345 kV and Above*, 2nd ed. Palo Alto, CA, USA: EPRI, 1982.
[34] *IEEE Standard Procedures for Measurement of Power Frequency Electric and Magnetic Fields From AC Power Lines*, IEEE Std. 664, 1994 (Reaffirmed 2008).
[35] W. Yao *et al.*, "A novel method for phasor measurement unit sampling time error compensation," *IEEE Trans. Smart Grid*, 2017, to be published. DOI: 10.1109/TSG.2016.2574946.
[36] H. A. Darwish and M. Fikri, "Practical considerations for recursive DFT implementation in numerical relays," *IEEE Trans. Power Del.*, vol. 22, no. 1, pp. 42–49, Jan. 2007.
[37] J. Zhao, L. Zhan, Y. Liu, H. Qi, J. R. Garcia, and P. D. Ewing, "Measurement accuracy limitation analysis on synchrophasors," in *Proc. IEEE Power Energy Soc. Gen. Meeting*, Denver, CO, 2015, pp. 1–5.
[38] G. B. Iyyuni and S. A. Sebo, "Study of transmission line magnetic fields," in *Proc. 22nd Annu. North Amer.*, Oct. 1990, pp. 222–231.
[39] Z. Lin *et al.*, "Application of wide area measurement systems to islanding detection of bulk power systems," *IEEE Trans. Power Syst.*, vol. 28, no. 2, pp. 2006–2015, May 2013.
[40] G. Zheng, Y. Liu, and G. Radman, "Wide area frequency based generation trip event location estimation," in *Proc. IEEE Power Energy Soc. Gen. Meeting*, San Diego, CA, 2012, pp. 1–6.

Wenxuan Yao (S'14) received the B.S. and Ph.D. degrees in electrical engineering from Hunan University, Changsha, China, in 2011 and 2017, respectively. He is working toward the Ph.D. degree in the Department of Electrical Engineering and Computer Science, University of Tennessee, Knoxville, TN, USA.

His research interests include wide-area power system monitoring, synchrophasor measurement applications, embedded system development, power quality diagnosis, and big data analysis for the power system.

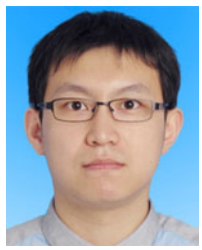

Haoyang Lu (S'15) received the B.E. degree from Hangzhou Dianzi University, Hangzhou, China, in 2010, and the M.E. degree from the University of Chinese Academy of Sciences, Beijing, China, in 2013, both majoring in electrical engineering. Currently, he is working toward the Ph.D. degree in the Department of Electrical Engineering and Computer Science, University of Tennessee, Knoxville, TN, USA.

His research interests include smart grid and communication system.

Micah J. Till (S'13) received the B.S. degree from Tennessee Technological University, Cookeville, TN, USA, in 2011, and the M.S. and Ph.D. degrees from the University of Tennessee, Knoxville, TN, USA, in 2015 and 2017, respectively, all in electrical engineering.

He works with Dominion Energy Virginia's Transmission System Protection Analysis Group, Richmond, VA, USA. His research interests include wide-area power system modeling, high-impact event scenarios, and phasor measurement unit applications.

Wei Gao (M'05) received the B.E. degree in electrical engineering from the University of Science and Technology of China, Hefei, China, in 2005, and the Ph.D. degree in computer science from Pennsylvania State University, State College, PA, USA, in 2012.

He is currently an Assistant Professor in the Department of Electrical Engineering and Computer Science, University of Tennessee, Knoxville, TN, USA. His research interests include wireless and mobile network systems, mobile cloud computing, mobile social networks, and cyber-physical systems.

Yilu Liu (S'88–M'89–SM'99–F'04) received the B.S. degree from Xi'an Jiaotong University, Xi'an, China, and the M.S. and Ph.D. degrees from the Ohio State University, Columbus, OH, USA, in 1986 and 1989, respectively, all in electrical engineering.

She is currently the Governor's Chair Professor with the University of Tennessee (UTK), Knoxville, TN, USA, and Oak Ridge National Laboratory (ORNL), Oak Ridge, TN, USA. Prior to joining UTK/ORNL, she was a Professor with Virginia Tech. She leads the effort to create the North American power grid Frequency Monitoring Network at Virginia Tech, which is now operated at UTK and ORNL as GridEye. Her current research interests include power system wide-area monitoring and control, large interconnection-level dynamic simulations, electromagnetic transient analysis, and power transformer modeling and diagnosis.

Dr. Liu is a member of the U.S. National Academy of Engineering.